Molecular Cell, Volume *84*

Supplemental information

Resolution of transcription-induced hexasome-nucleosome complexes by Chd1 and FACT

Maik Engeholm, Johann J. Roske, Elisa Oberbeckmann, Christian Dienemann, Michael Lidschreiber, Patrick Cramer, and Lucas Farnung

Supplemental Information

Resolution of Transcription-Induced Hexasome-Nucleosome Complexes by Chd1 and FACT

Maik Engeholm[1], Johann J. Roske[1, 2], Elisa Oberbeckmann[1], Christian Dienemann[1], Michael Lidschreiber[1], Patrick Cramer[1], and Lucas Farnung[1, 3]

[1] *Max Planck Institute for Multidisciplinary Sciences, Am Fassberg 11, Göttingen, 37077, Germany*
[2] *MRC Laboratory of Molecular Biology, Francis Crick Avenue, Cambridge, CB2 0QH, UK*
[3] *Harvard Medical School, Blavatnik Institute, Department of Cell Biology, 240 Longwood Avenue, Boston, 02115, MA, USA*

September 3, 2024

Contents

1 Supplemental Figures **2**
Figure S1 - DNA fragments 2
Figure S2 - Hexasome-nucleosome complexes at genes with low transcriptional output 4
Figure S3 - Hexasome-nucleosome peaks with a twofold higher concentration of MNase 5
Figure S4 - The CHD4-bound SHN103 . . 6
Figure S5 - Comparison between the structures of SHN103 and DN103 7
Figure S6 - The unbound SHN103 9
Figure S7 - The Chd1-bound mononucleosome 11
Figure S8 - Remodelling assay - native gels 12
Figure S9 - Remodelling assay - site-directed mapping 13
Figure S10 - Dimer deposition by FACT onto free DNA and nucleosomes 15
Figure S11 - Recombinant proteins, nucleosomal reconstitutions and grafix gradients 17
Figure S12 - Image processing unbound SHN103 19
Figure S13 - Image processing Chd1-bound SHN103 21
Figure S14 - Image processing Chd1-bound DN103 23
Figure S15 - Image processing Chd1-bound 30W54 25
Figure S16 - FSC curves and angular distributions 27

2 Supplemental Tables **29**
Table S1 - Cryo-EM statistics for SHN103 unbound and SHN103:Chd1 30
Table S2 - Cryo-EM statistics for DN103:Chd1 and 30W54:Chd1 32
Table S3 - Geometry of SHN103 in the different structures 33

3 References **34**

1 Supplemental Figures

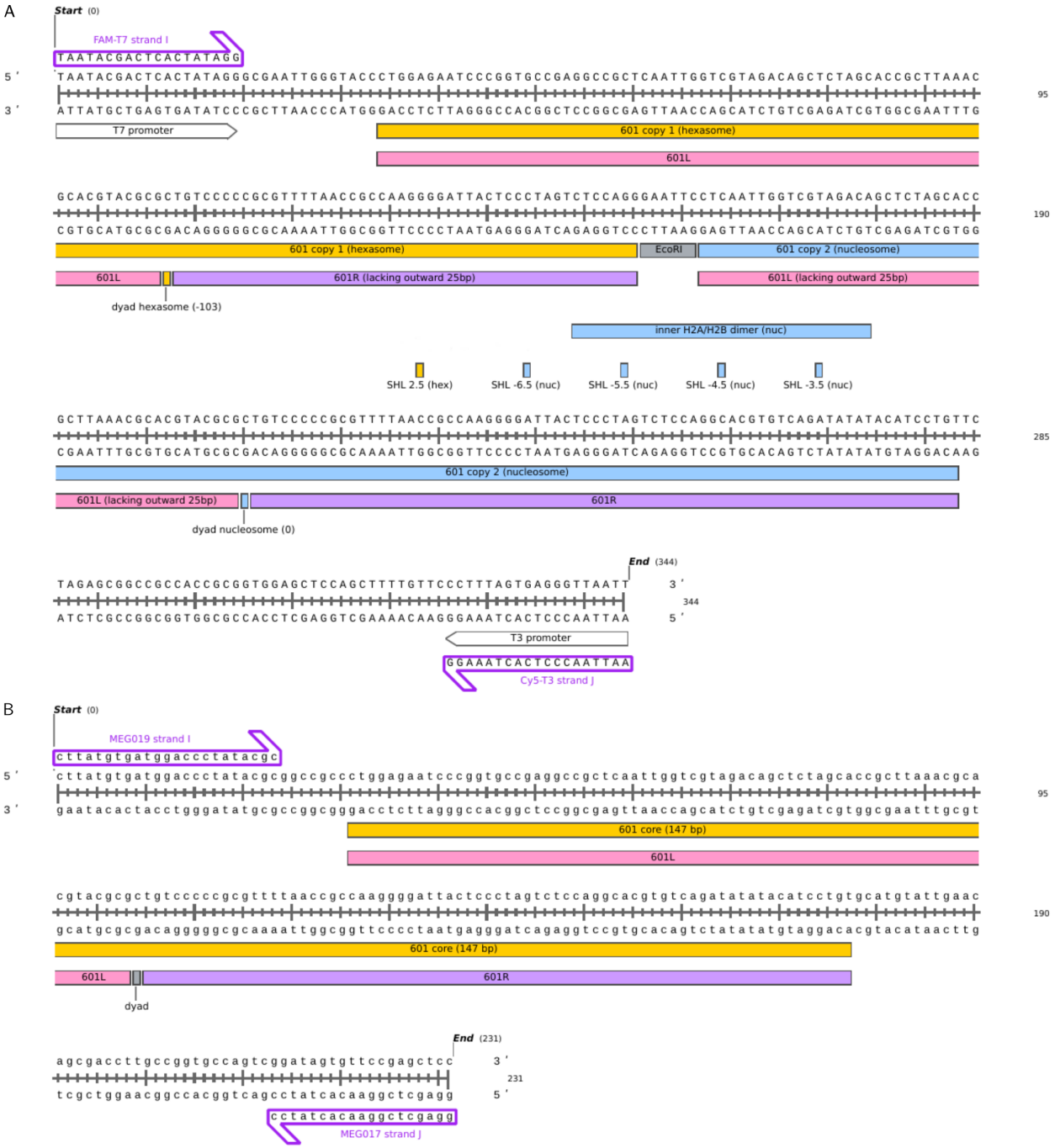

Figure S1: **DNA fragments used in this study, related to STAR Methods.** (**A**) Sequence of the 344-bp fragment used to reconstitute SHN103. The two truncated copies of the 601 positioning sequence are indicated in orange and light blue colour. The nomenclature of the 601 half sequences follows McGinty and Tan [1]. 601L is also commonly referred to as the TA-rich half. The nucleosome is reconstituted on the copy of the 601 sequence that is facing inwards with its truncated 601L half, the hexasome on the other one. The position of the inward-facing H2A/H2B dimer of the nucleosome is indicated, as are the positions of SHL -3.5 to -6.5 of the nucleosome and SHL 2.5 of the hexasome. The top strand corresponds to strand I in the pdb file and carries the FAM label in the site-directed mapping experiments. (**B**) Sequence of the 231-bp DNA fragment used to reconstitute 30W54. Annotations are as in (A). Images were prepared using *SnapGene software (www.snapgene.com).*

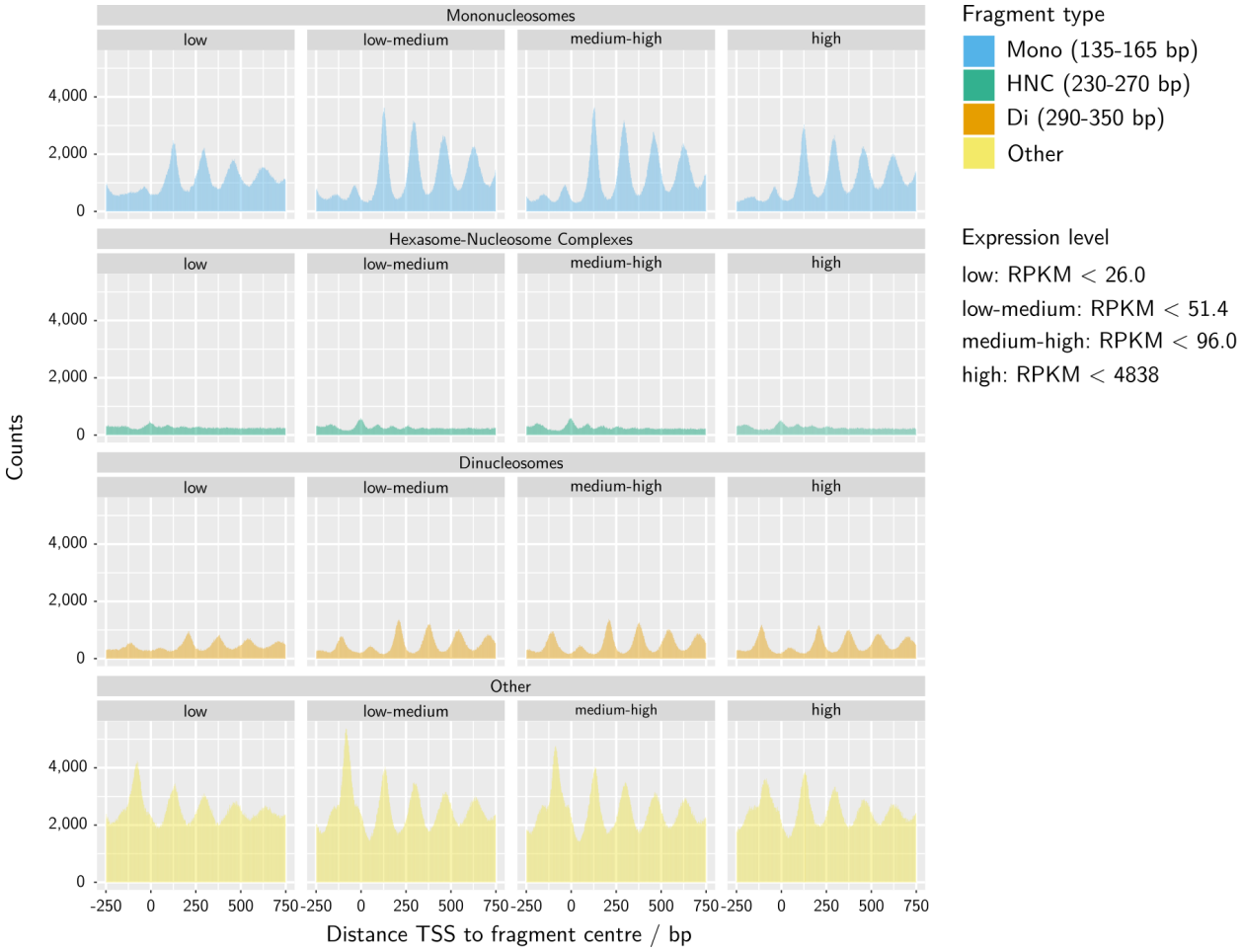

Figure S2: **Hexasome-nucleosome complexes are less prominent at genes with low transcriptional output, related to Figure 1.** CCC-Seq fragments from Henikoff et al.[2] were binned as in Figure 1B. For the 4909 protein coding genes for which a TSS has been mapped by Pelechano et al.[3], RPKMs were calculated from published 4tU-Seq data[4] (GSM2516273 and GSM2516274). Genes were then divided into quartiles with RPKM cutoffs as indicated, and for each fragment type and quartile, fragment centre positions were aligned at the TSS to create metagene plots. In the group of the most lowly expressed genes hexasome-nucleosome peaks are less prominent compared to more highly transcribed genes, confirming that hexasome-nucleosome complexes are part of the nucleosome organisation of actively transcribed genes. Note that even genes within the low-expression quartile show detectable levels of transcription, which is required to determine the position of the TSS.

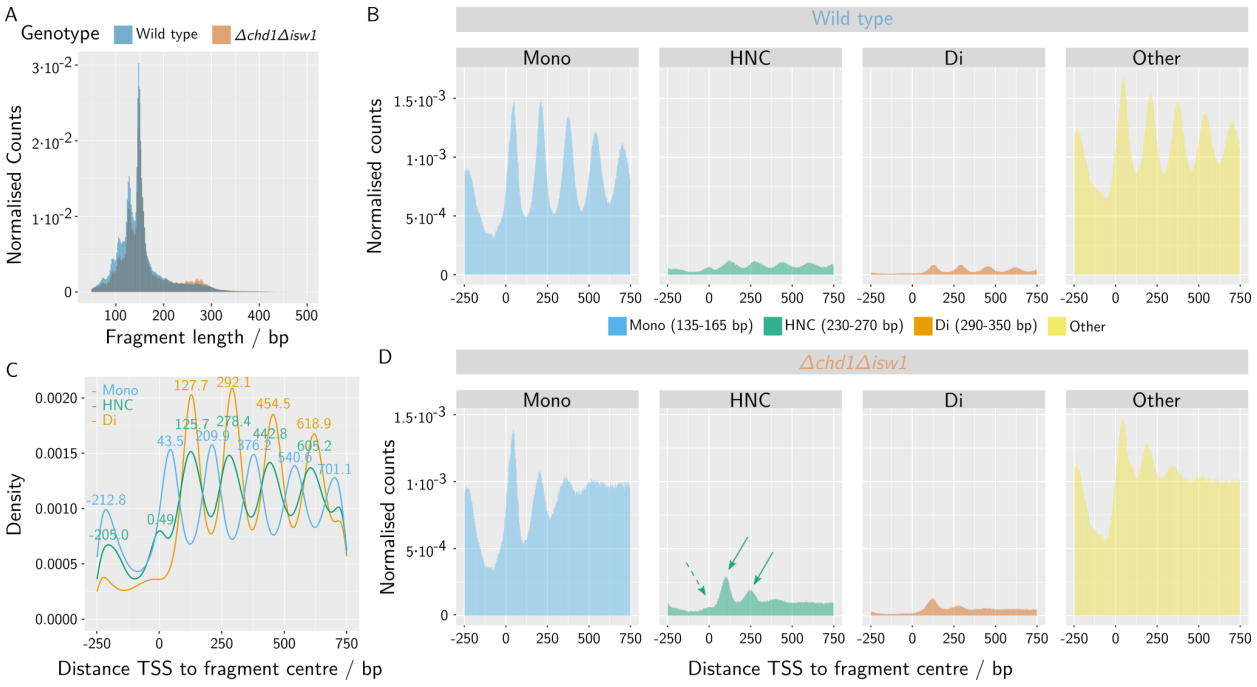

Figure S3: **Hexasome-nucleosome peaks are reproduced with a twofold higher concentration of MNase, related to Figure 2.** While the MNase-Seq data presented in Figure 2 were generated using 25 U of MNase per reaction, the study by Ocampo et al. [5] also includes a second dataset using 50 U of MNase instead, which is presented here. (**A**) Length distributions of MNase-Seq fragments obtained from wild-type (blue) and *chd1*Δ*isw1*Δ knock-out (orange) cells. (**B**) Fragments were binned as indicated. For each bin, the centre positions of fragments were aligned at the TSS of the same 4909 protein coding genes as in Figure 1 and 2. (**C**) Kernel density plots of the data in (B). Positions of individual peaks are indicated. (**D**) MNase-Seq fragments obtained from *chd1*Δ*isw1*Δ knock-out cells were binned and plotted in the same way as the wild-type data in (B). Green arrows denote the hexasome-nucleosome peaks at 126 and 278 bp, whose height increases in the knock-out. The dashed arrow indicates the hexasome-nucleosome peak at the TSS, whose height does not increase.

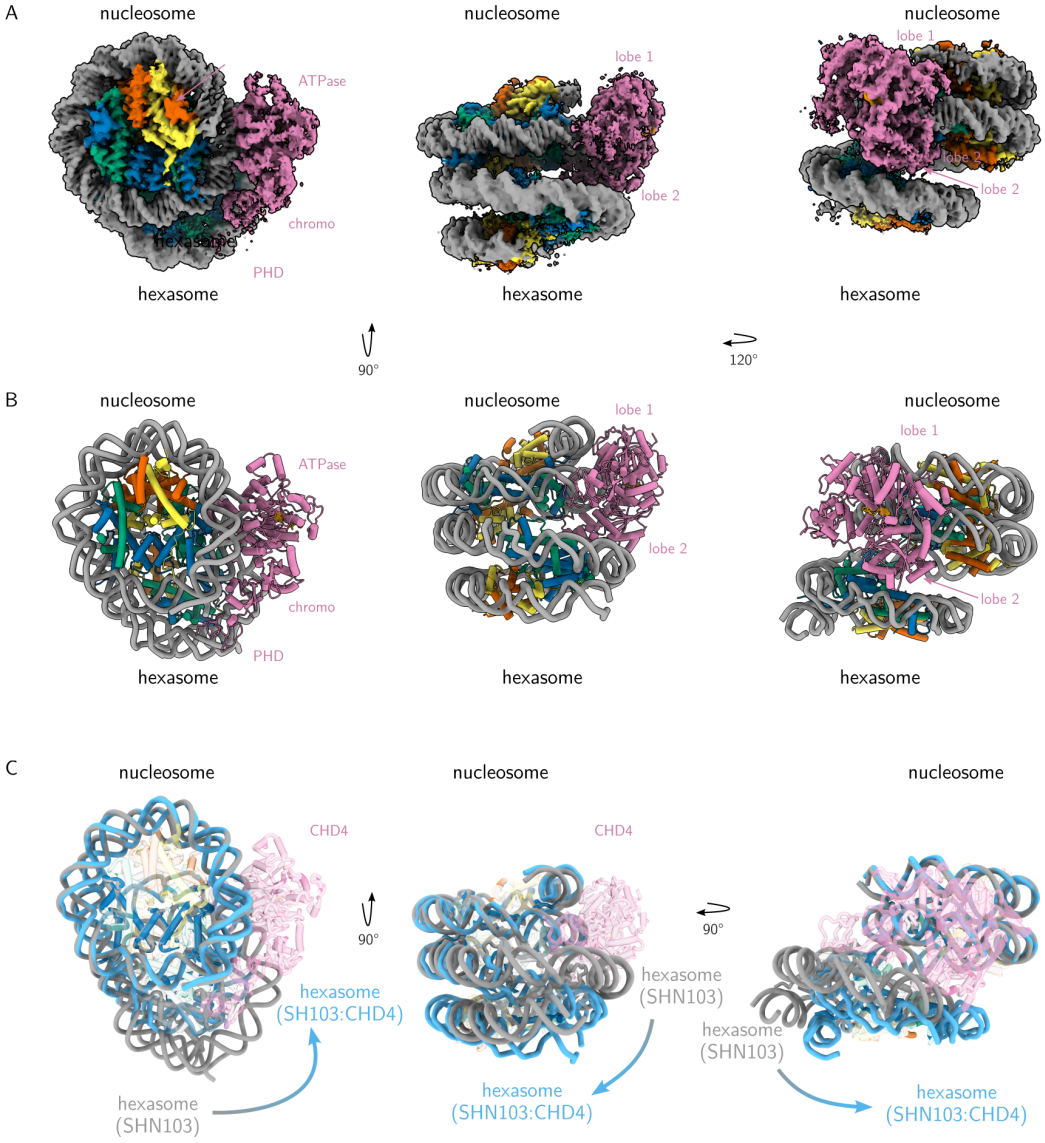

Figure S4: **CHD4 binds to the nucleosome portion of SHN103, related to Figure 3.** (**A and B**) Structure of the CHD4-bound SHN103 viewed along the nucleosomal superhelical axis (left) or dyad axis (middle) and as indicated (right). Shown are Coulomb potential maps (A) and representations of an atomic model (B). (**C**) Differences in the geometry of SHN103 when compared between the CHD4-bound (coloured) and the unbound structure (grey). The two structures are aligned by the central portion of the nucleosomal DNA, and the view is along the nucleosomal superhelical axis (left), dyad axis (middle) or perpendicular to both axes (right). Arrows denote the movement of the hexasome from its position in the unbound SHN103 to that within the CHD4-bound structure.

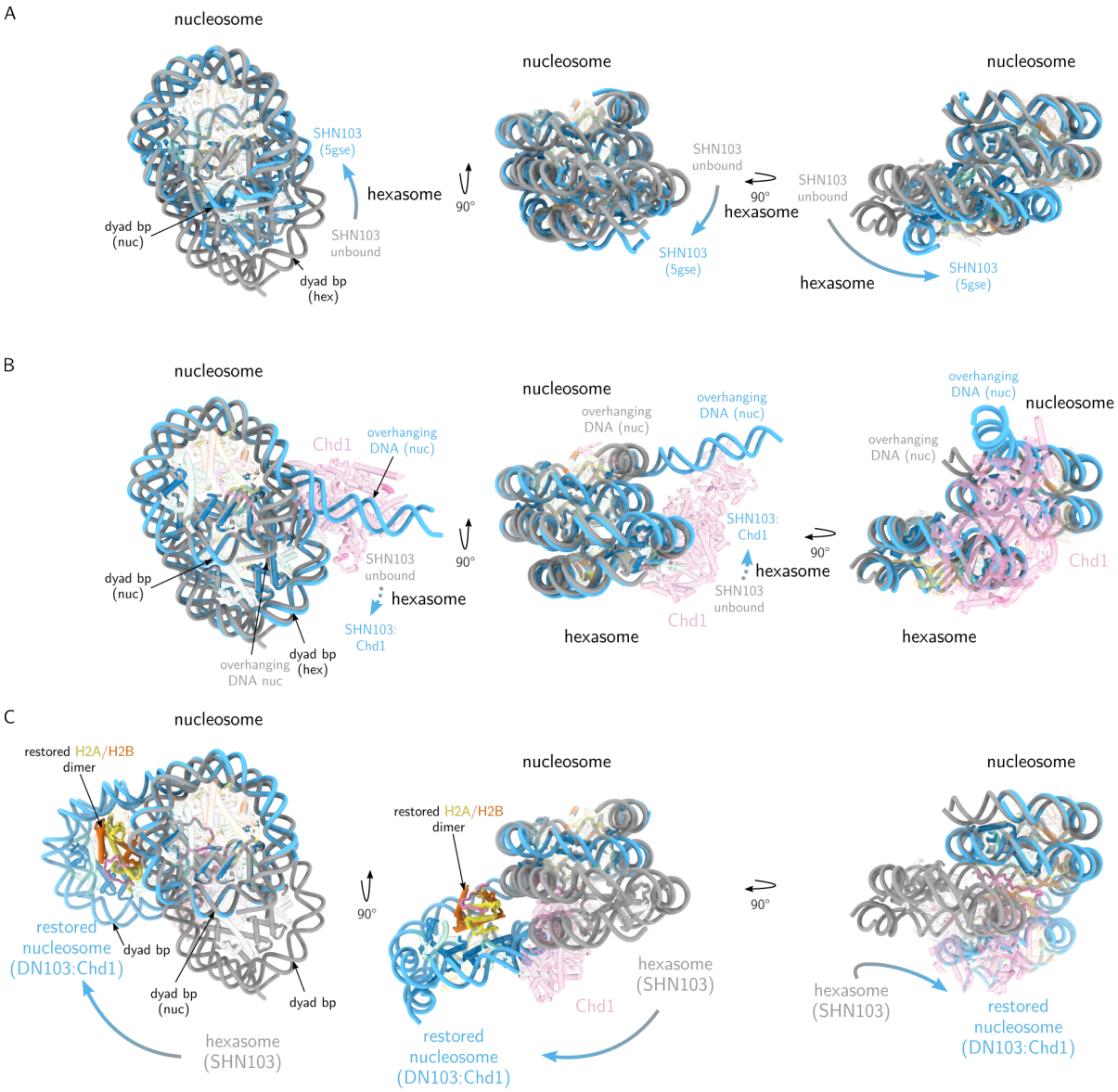

Figure S5: **Conformational changes between the different structures of SHN103 and DN103, related to Figures 3, 4 and 5.** Shown are **(A)** a previous crystal structure of SHN103[6] (PDB-5GSE), **(B)** the Chd1-bound SHN103 as in Figure 4, and **(C)** the Chd1-bound DN103 as in Figure 5, relative to the unbound SHN103 (Figure 3) as a common reference. The structure of the unbound SHN103 is always shown in grey and the respective other study in colour (DNA in light blue). In each panel, the two structures are aligned by the central portion of the nucleosomal DNA, and the view is along the nucleosomal superhelical axis (left), dyad axis (middle) or perpendicular to both axes (right). Histone proteins and Chd1 are shown in transparent shading except for histone H3 to indicate the position of the dyad base pair and the reinstalled

H2A/H2B dimer in (C). Arrows denote the movement of the hexasome from its position in the unbound SHN103 to that in the respective other structure. Only minimal changes occur upon Chd1 binding (B).

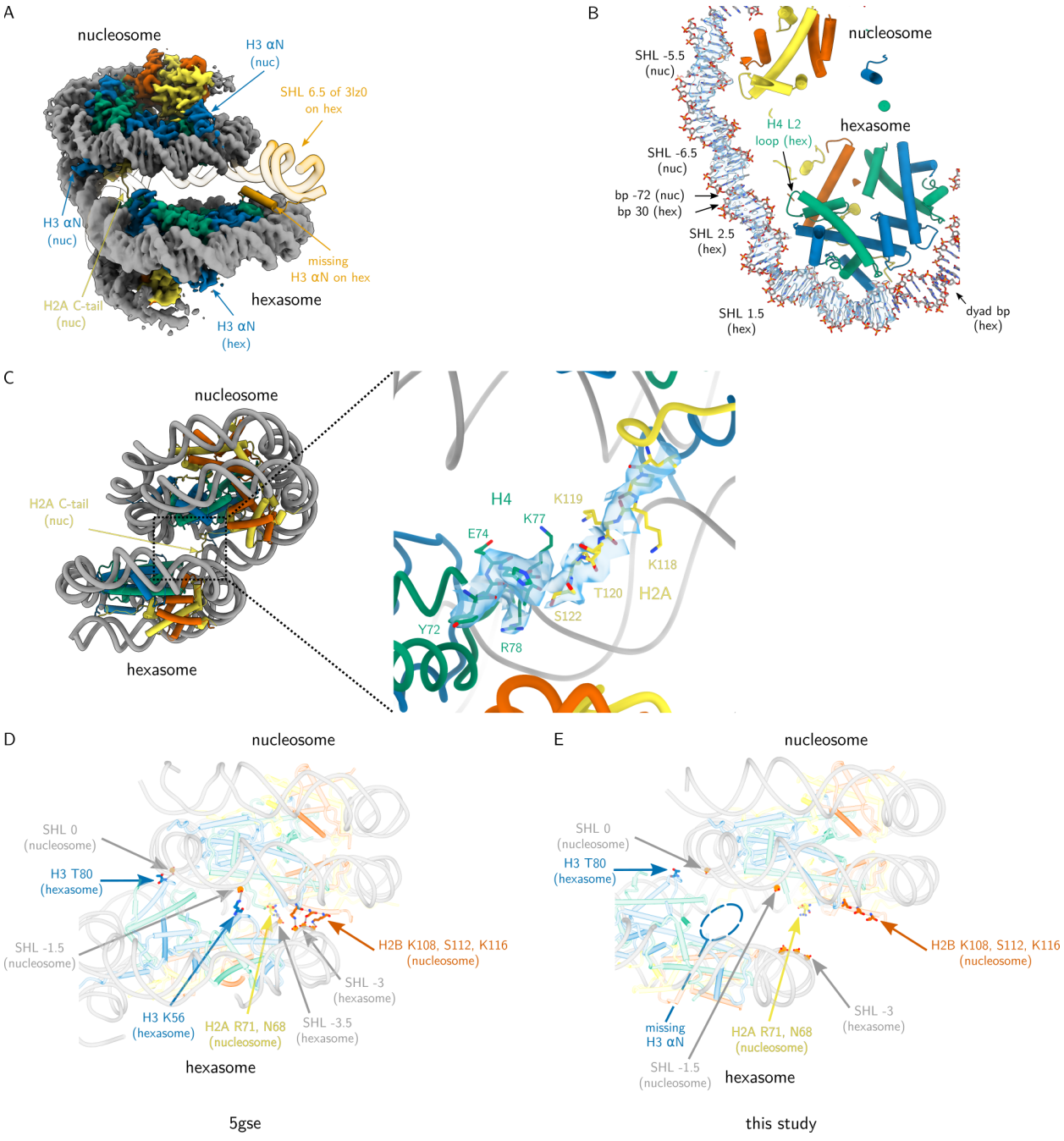

Figure S6: **Additional aspects of the SHN103 structure, related to Figure 3.** (**A**) On the inward-facing end of the hexasome, a density corresponding to the N-terminal α-helix of histone H3 is missing. Parts of a model of a mononucleosome on the 601 sequence[7] (PDB-3LZ0, orange colour) were superimposed

onto the hexasome portion of SHN103 to illustrate the position of the N-terminal α-helix and of the outmost 10 bp of the nucleosomal DNA. (**B**) Path of the linker DNA in between the nucleosome and hexasome. The Coulomb potential maps corresponding to base pairs -51 to -72 of the nucleosomal DNA and base pairs 7 to 30 of the hexasomal DNA are shown as transparent surfaces. (**C**) Stabilising interactions between the nucleosome- and hexasome portion of SHN103 are formed by the H2A C-terminal tail emanating from the inward-facing H2A/H2B dimer of the nucleosome. This tail runs from the bottom surface of the nucleosome towards the L2-loop of the inward-facing copy of H4 of the hexasome. Overview (left) and detail view (right). The Coulomb potential maps corresponding to the H2A C-terminal tail and the H4 L2 loop are shown as transparent surfaces. Note that within a mononucleosome, the H4 L2-loop mediates contacts to the nucleosomal DNA at SHL 2.5 (ref. 8). In the context of SHN103, however, this section of the hexasomal DNA has detached from the octamer surface to contribute to the linker segment (Figure 3D and panel B this figure). This makes the H4 L2-loop available for interactions with the H2A C-terminal tail. **(D and E)** The interface between the hexasome and nucleosome in our structure (E) as compared to a previous crystal structure of SHN103 (ref. 6, PDB-5GSE, D). Shown are representations of an atomic model; view is from the side of SHN103 facing away from the linker. In the crystal structure seven histone residues are found at a suitable distance to form hydrogen bonds to the DNA of the respective other particle (shown as sticks in D with their partner DNA phosphates as balls). This includes five residues at the back of the inward-facing H2A/H2B dimer of the nucleosome (H2A:N68, H2A:R71, H2B:K108, H2B:S112 and H2B:K116) as well as two at the front of the H3/H4 tetramer of the hexasome (H3:K56 and H3:T80). Changing these amino acids to alanine or glutamate results in an increased radius of gyration as determined by SAXS and, therefore, likely destabilises SHN103 in solution[6]. Interestingly, this effect appears to be largely mediated by the two amino acids on H3, as mutating the five amino acids on H2A/H2B only has virtually no effect. In our structure (E) these residues are not at hydrogen-bonding distance to the DNA of the other particle but are highlighted in the same way as in (D). In particular, the five residues at the rear of the nucleosomal H2A/H2B dimer are more than 15 Å away from the hexasomal DNA, due to the outward rotation and forward shift of the hexasome. Moreover, H3:K56 (which is located on the N-terminal α-helix of H3) is not resolved in our structure. Nevertheless, the high degree of conformational flexibility as shown in Videos 2 and 3, together with the mutational analysis by Kato et al.[6] suggest that these (and possibly other) residues are *transiently* engaged in trans-particle histone-DNA contacts and stabilise the stacked conformation of SHN103.

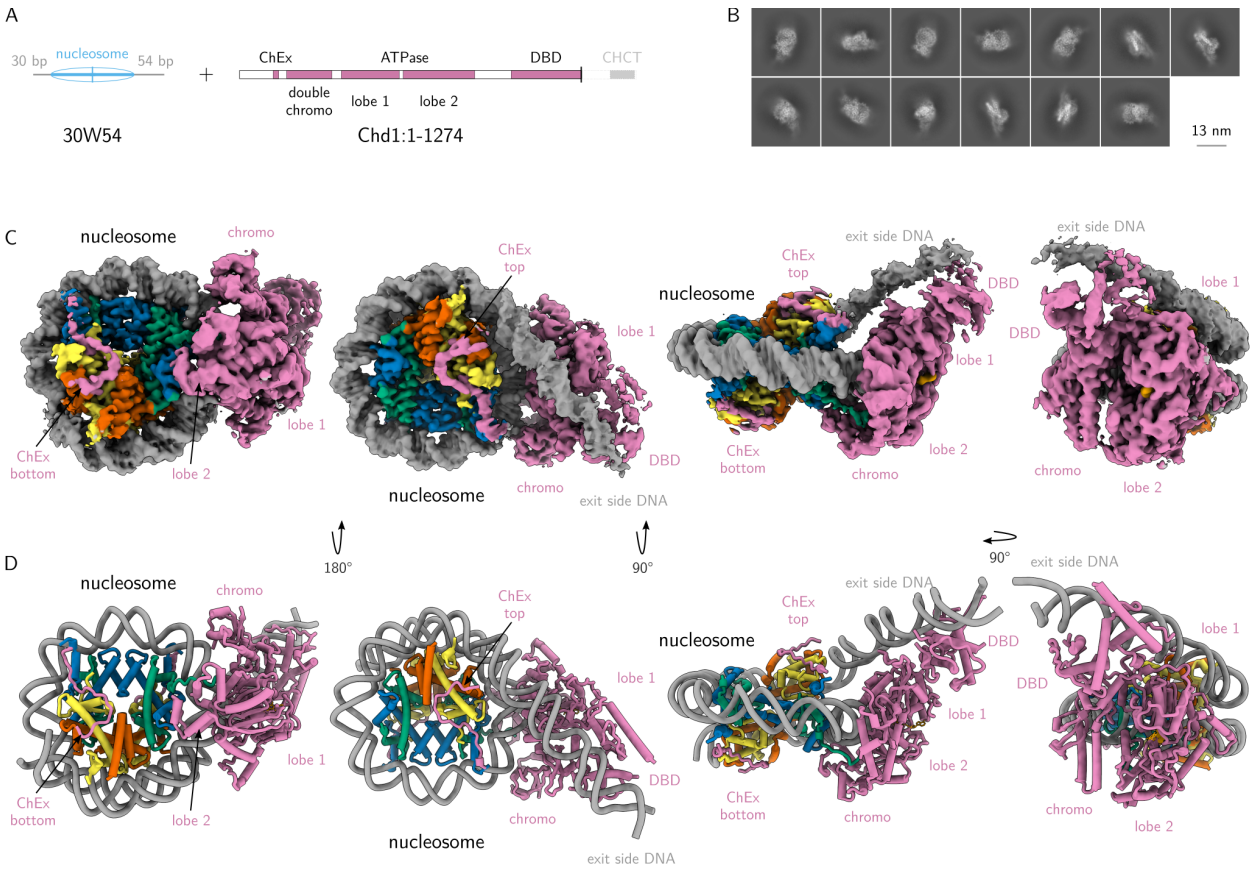

Figure S7: **Structure of a Chd1-bound mononucleosome, related to Figure 4.** Structure of a Chd1-bound mononucleosome with one copy of Chd1 and the DBD bound to the exit DNA, which was used as a comparator for the interface between the DBD and the ATPase- and chromodomain in Figure 4E. (**A**) Schematic representation of 30W54 and domain organisation of the C-terminally truncated Chd1 (Chd1:1-1274). (**B**) 2D classes obtained from the final class of the Chd1-bound 30W54 with one copy of Chd1 and the DBD bound to the exit DNA. (**C and D**) Structure of the Chd1-bound 30W54 viewed along the superhelical axis (left and second from left) or dyad axis (second from right) and perpendicular to both axes (right). Shown are Coulomb potential maps (C) and representations of an atomic model (D). Note that a density corresponding to ChEx is present on both H2A/H2B dimers. These densities may either correspond to alternative conformations of ChEx, similar to the situation in Figure 5F, which would imply that ChEx is not restricted to binding to the exit-side dimer but may also reach to the entry side. Alternatively, the density on the entry-side dimer may belong to a second copy of Chd1 that was originally bound to the other SHL2 (as observed in other classes from this dataset) but was lost during the process of grid preparation.

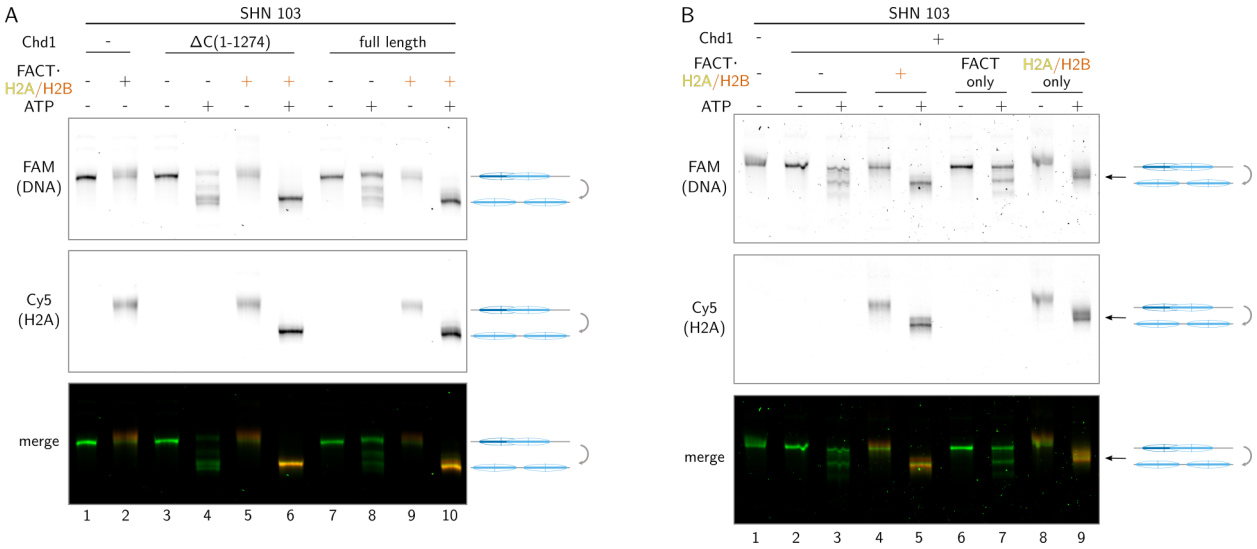

Figure S8: **Restoration of the missing dimer by FACT stimulates Chd1 remodelling, related to Figure 6.** (**A**) SHN103 (100 nM) was remodelled by either full-length (lanes 7-10) or a truncated version of Chd1 (amino acids 1-1274, lanes 3-6) at a concentration of 10 nM each in the presence or absence of FACT that had been preincubated with a fluorescently labelled H2A/H2B dimer (100 nM). ATP was added as indicated. Reaction products were resolved by native PAGE, and the FAM-labelled DNA (top, green colour in the merge) and Cy5-labelled H2A (middle, red colour in the merge) were visualised separately. In the absence of FACT, remodelling by Chd1:1-1274 is slightly more efficient than with full-length Chd1 (compare lanes 4 and 8). Following restoration of the H2A/H2B dimer, however, in either case virtually the entire population of template molecules are converted into a single product band (lanes 6 and 10). (**B**) SHN103 (100 nM) was remodelled by full-length Chd1 (50 nM) in the presence or absence of FACT that had been preincubated with a fluorescently labelled dimer (lanes 2-5). Additional controls include FACT that has not been incubated with a dimer (lanes 6 and 7) and a Cy5-labelled dimer without FACT (lanes 8 and 9). ATP was added as indicated. Reaction products were resolved by native PAGE as in (A). While in the absence of FACT only a fraction of SHN103 is remodelled, with the addition of dimer-charged FACT virtually the entire population is converted into a single product species that has incorporated the labelled dimer (compare lanes 3 and 5). Upon addition of FACT only, no clear stimulation of remodelling does occur (compare lanes 3 and 7), indicating that the activation of Chd1 depends on the restoration of the missing dimer rather than on a direct interaction with FACT. Addition of the H2A/H2B dimer only (without FACT), gives rise to rather blurred bands, that migrate slower than the product band in lane 5 (arrow).

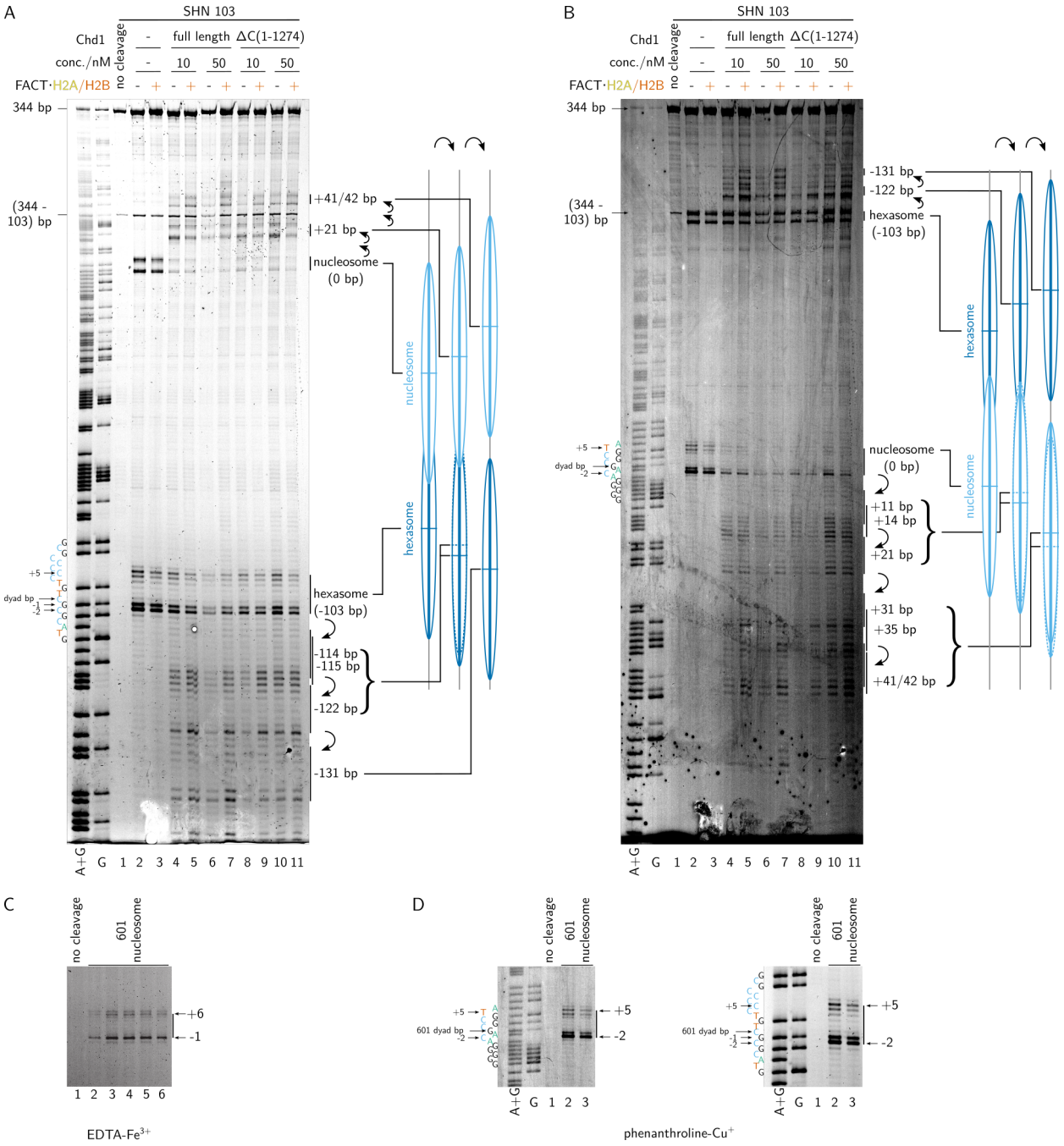

Figure S9: **Restoration of the H2A/H2B dimer by FACT stimulates repositioning by Chd1, related to Figure 6.** (**A and B**) SHN103 (100 nM) with a FAM label on the hexasome end of the DNA and a Cy5 label on the nucleosome end was remodelled using either full-length (lanes 4-7) or a truncated

version of Chd1 (amino acids 1-1274, lanes 8-11) at different concentrations as indicated and in the presence or absence of dimer-charged FACT (100 nM). To determine nucleosome positions site-directed hydroxyl-radical mapping was used, and samples were run on a denaturing gel, along with Maxam-Gilbert sequencing reactions as a marker. Shown are a FAM scan (A) and a Cy5 scan (B) of the same gel. Translational positions inferred from the mapping are indicated on the schematic representations of template molecules on the right-hand side. Arrows denote movements of the hexasome/nucleosome along the DNA. The band at 344 bp - 103 bp = 241 bp, which is also present in the no-cleavage control, is due to the polymerase skipping one copy of the 601 sequence when PCR-amplifying the dimeric tandem-repeat DNA fragment. Under virtually all conditions repositioning of both the original nucleosome and the hexasome/restored nucleosome proceeds further in the presence of dimer-charged FACT (compare neighbouring lanes within individual pairs). (**C and D**) Differences between the mapping signals obtained with (EDTA-2-aminoethyl) 2-pyridyl disulfide-Fe^{3+} and phenathroline-Cu^{+} attached to H4:S47C. With EDTA-Fe^{3+} the mapping signal comprises a major cut 1 bp upstream of the dyad and two minor cuts 6 and 7 bp downstream as originally reported[9] (C). With phenathroline-Cu^{+}, cleavage occurs at two positions upstream of the dyad (-2 bp > -1 bp) and several downstream positions, the strongest of which is found at +5 bp (D). Stronger cleavage at -2 bp than at -1 bp is in agreement with the results of a molecular dynamics simulation of phenathroline-Cu^{+} attached to H4:S47C[2].

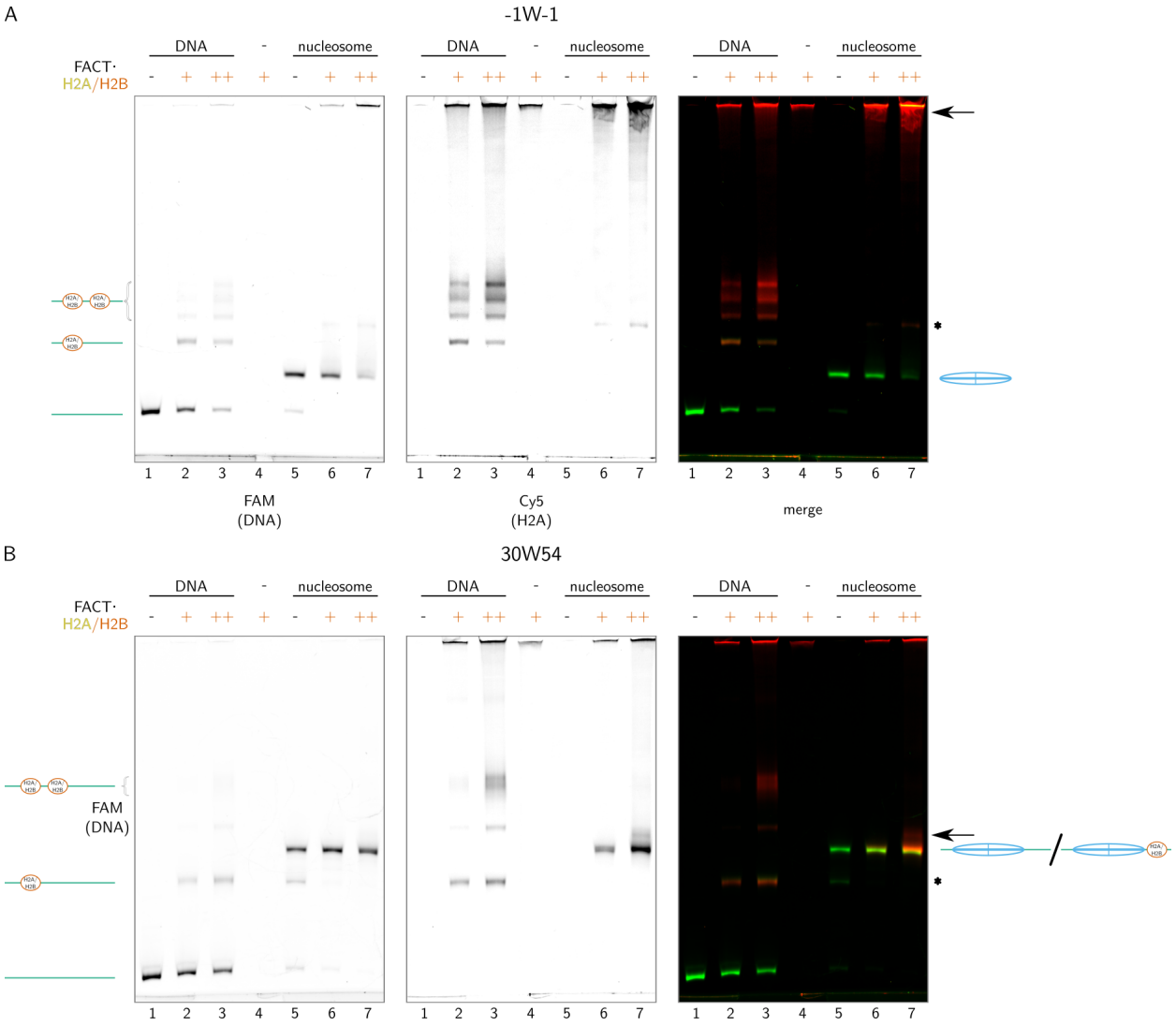

Figure S10: **Deposition of H2A/H2B dimers by FACT onto free DNA and nucleosomes, related to Figure 6.** (**A and B**) A 145-bp and a 231-bp DNA fragment based on the 601 sequence were reconstituted into an NCP (-1W-1, A) and a nucleosome (30W54, B), respectively. The histone-free DNA fragments (lanes 1-3) and the NCP/nucleosome (lanes 5-7), at a concentration of 100 nM each, were incubated with FACT·H2A/H2B at a concentration of 100 nM (+) or 200 nM (++). Otherwise, reaction conditions were identical to the remodelling assay in Figures 6 and S8. With either DNA fragment, incubation with FACT gives rise to several slower migrating species that have incorporated the Cy5 label, indicating that FACT deposits one or more H2A/H2B dimers on the free DNA. No Cy5 label is incorporated into the NCP (A, lanes 6 and 7). Instead, in these lanes a large fraction of the signal is shifted to the wells, indicating that FACT·H2A/H2B may cause the NCP to form aggregates (arrow). In addition, lane A7 contains a weak band that has incorporated the Cy5 label but migrates differently from those observed with the free DNA

(*). The nucleosome with overhanging DNA, on the other hand, acquires Cy5 signal upon incubation with FACT without a clear change in its migration velocity (B, lane 6 and 7), which indicates an exchange of H2A/H2B dimers. The band indicated with the arrow might then correspond to a species, in which an additional H2A/H2B dimer has been deposited on the overhanging DNA. Taking into account the results in (A), however, it is also possible that FACT cannot exchange dimers under these conditions and that deposition of an additional dimer on 30W54 is not associated with a significant change in mobility. Further research is needed to resolve this issue. In panel (B), the asterisk indicates an additional species present in the original reconstitution that disappears upon incubation with dimer-charged FACT (lanes 5-7; also compare Figure S11E). Unlike what has been previously reported for human FACT [10], the FACT·H2A/H2B complex by itself does not enter the gel (A and B, lanes 4).

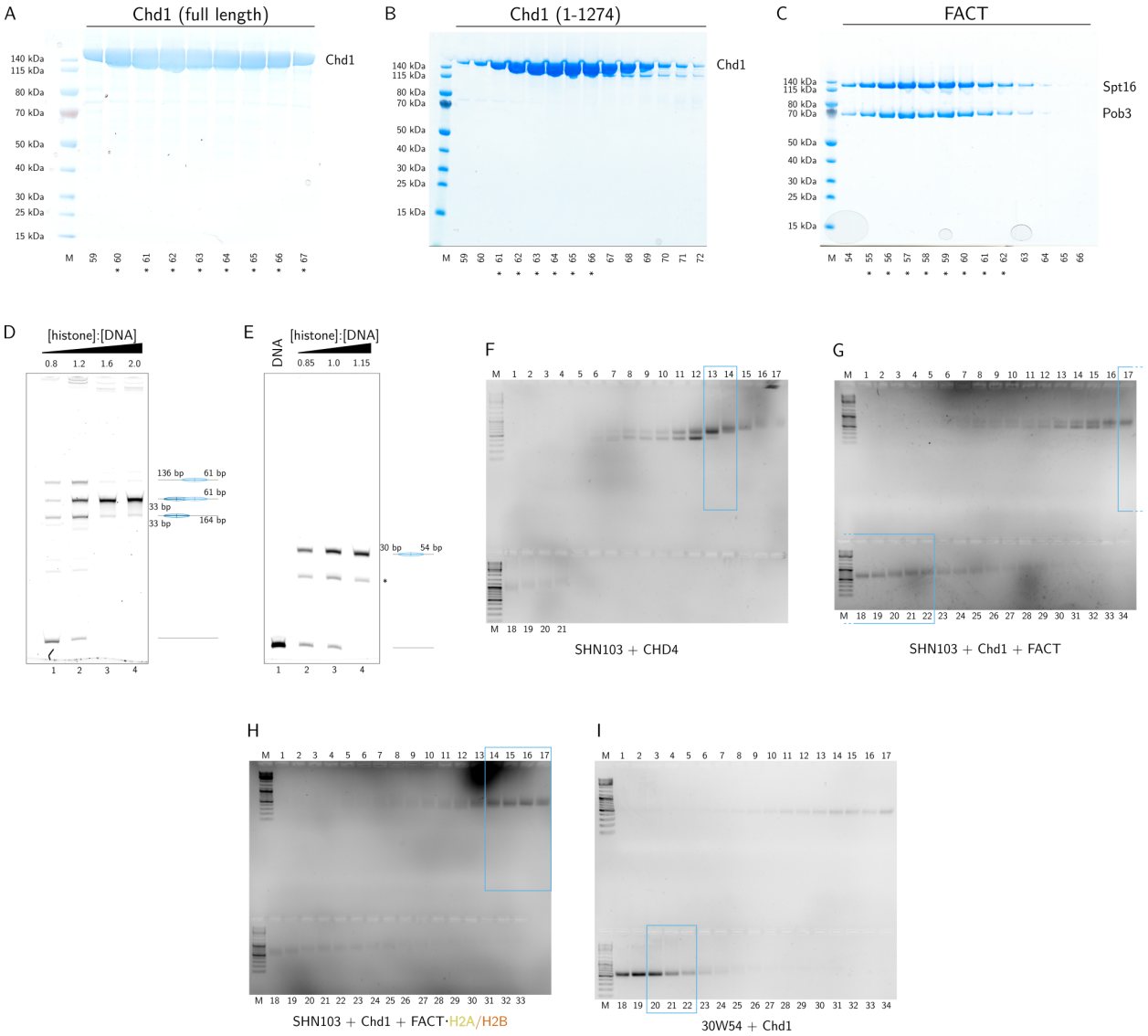

Figure S11: **Recombinant proteins, nucleosomal reconstitutions and grafix gradients, related to STAR Methods.** (**A-C**) Recombinant proteins and protein complexes were expressed in insect cells and purified as described in STAR Methods, including a final gel-filtration step on a HiLoad 16/600 Superdex 200 pg column. 1-ml fractions from these runs were run on a NuPAGE 4-12% Bis-Tris gel in MES buffer. Fractions marked with an asterisk were pooled, concentrated and snap frozen. (**D and E**) The 344-bp DNA fragment in Figure S1A (D) and the 231-bp fragment in Figure S1B (E) were mixed with an histone octamer at the indicated molar ratios, and salt-gradient dialysis was performed as described under STAR Methods to obtain nucleosomes. Positions of the various product species are indicated on the right-hand side. The band denoted with (*) is regularly observed when reconstituting 30W54. (**F-I**) Fractionation of grafix gradients. Grafix gradients were divided into fractions of ∼140 µl each, and 12 µl were run on a 2%

agarose gel. Fractions that were selected and pooled for preparing grids are indicated by the blue boxes.

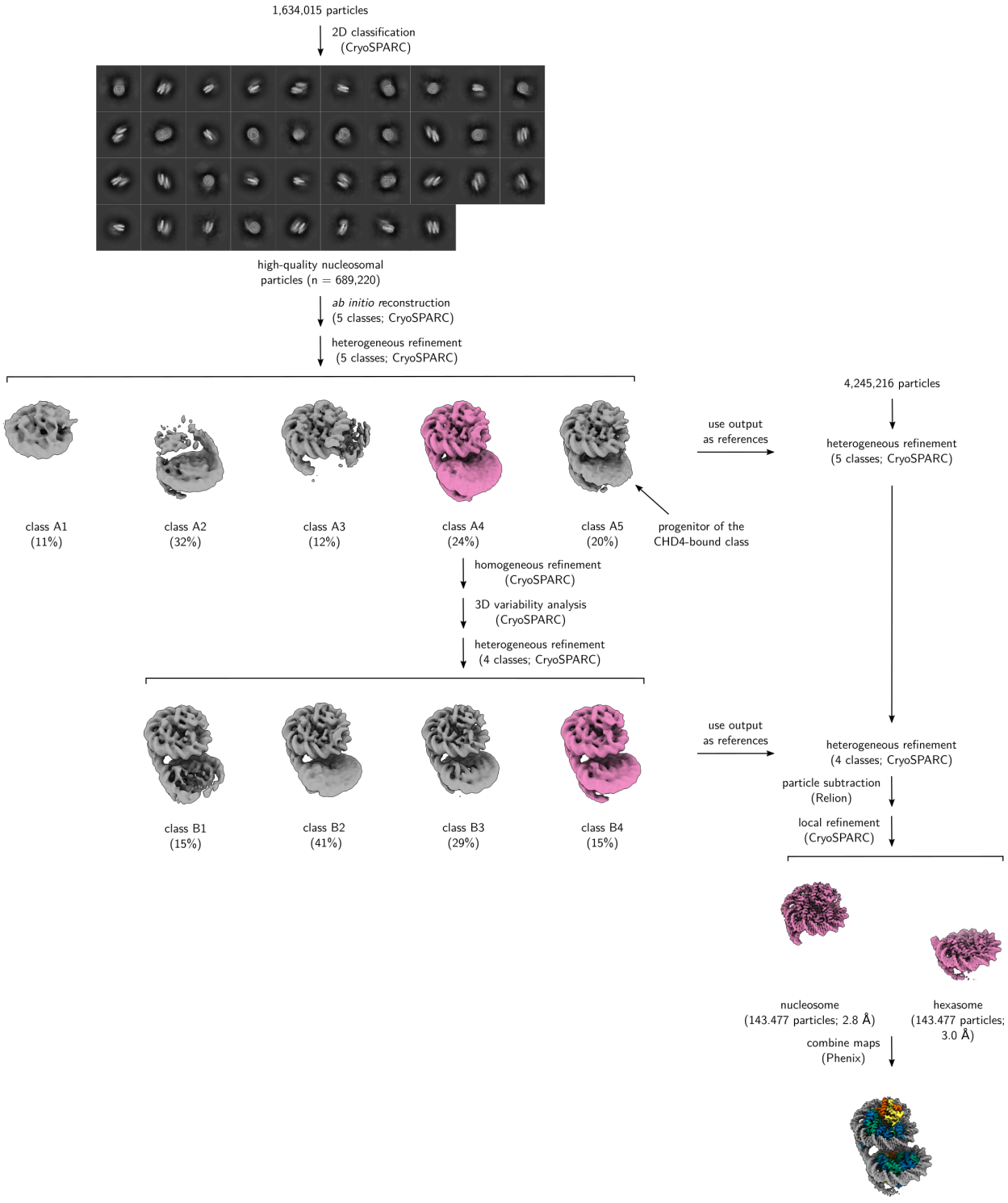
1,634,015 particles
2D classification
(CryoSPARC)
high-quality nucleosomal
particles (n = 689,220)
ab initio reconstruction
(5 classes; CryoSPARC)
heterogeneous refinement
(5 classes; CryoSPARC)
class A1
(11%)
class A2
(32%)
class A3
(12%)
class A4
(24%)
class A5
(20%)
progenitor of the
CHD4-bound class
use output
as references
4,245,216 particles
heterogeneous refinement
(5 classes; CryoSPARC)
homogeneous refinement
(CryoSPARC)
3D variability analysis
(CryoSPARC)
heterogeneous refinement
(4 classes; CryoSPARC)
class B1
(15%)
class B2
(41%)
class B3
(29%)
class B4
(15%)
use output
as references
heterogeneous refinement
(4 classes; CryoSPARC)
particle subtraction
(Relion)
local refinement
(CryoSPARC)
nucleosome
(143.477 particles; 2.8 Å)
hexasome
(143.477 particles;
3.0 Å)
combine maps
(Phenix)

Figure S12: **Image processing for the reconstruction of SHN103, related to Figure 3 and STAR Methods.** For this sample, SHN103 was incubated with human CHD4 in the presence of ADP·BeF_3. Further processing of class A5 yields a class in which CHD4 binds to the inward-facing SHL2 of the nucleosome. This causes a downward tilt of the hexasome, such that the geometry of the CHD4-bound SHN103 significantly differs from the unbound state. See STAR Methods for further explanation.

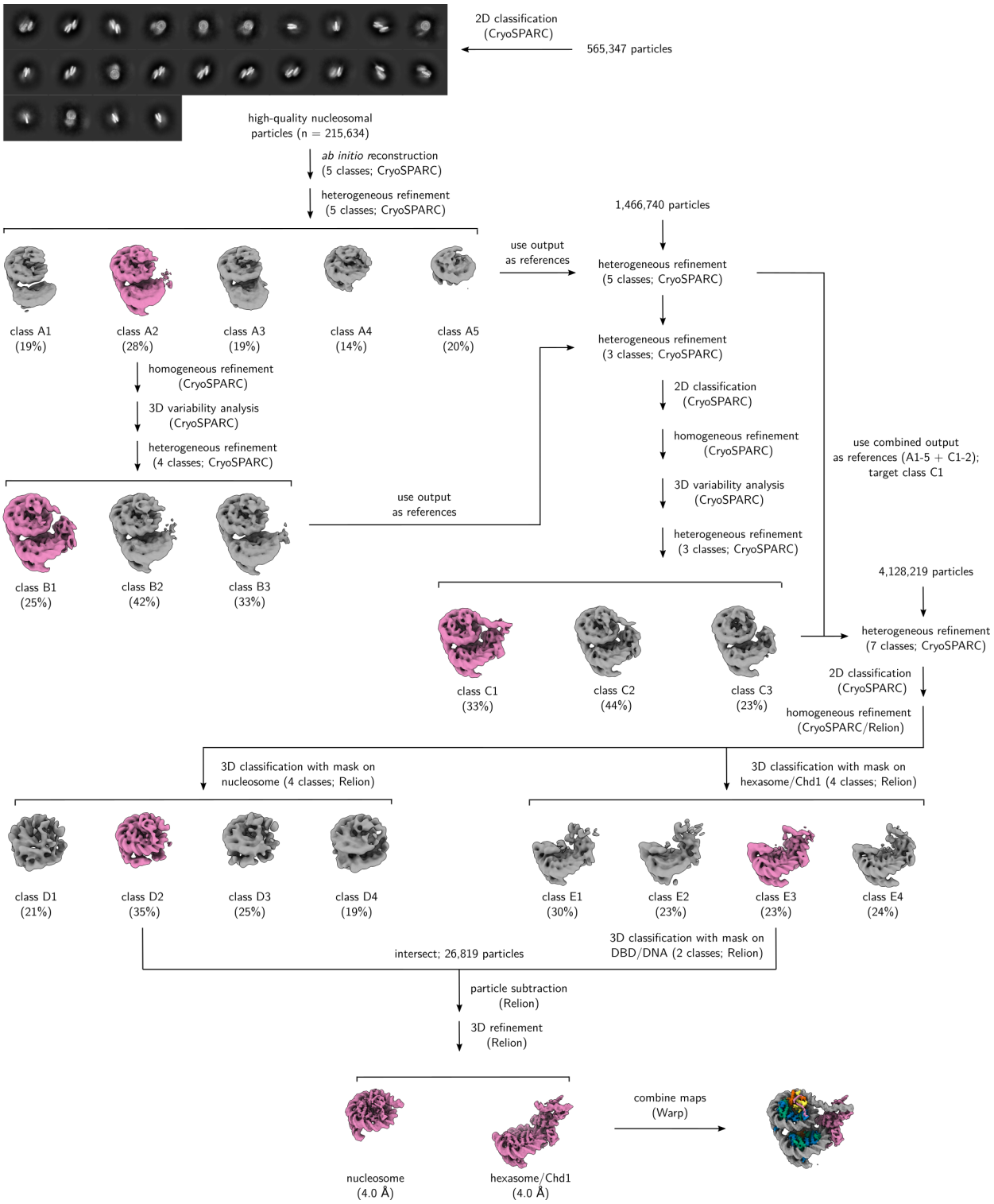
2D classification
(CryoSPARC)
565,347 particles
high-quality nucleosomal
particles (n = 215,634)
ab initio reconstruction
(5 classes; CryoSPARC)
heterogeneous refinement
(5 classes; CryoSPARC)
class A1
(19%)
class A2
(28%)
class A3
(19%)
class A4
(14%)
class A5
(20%)
use output
as references
1,466,740 particles
heterogeneous refinement
(5 classes; CryoSPARC)
heterogeneous refinement
(3 classes; CryoSPARC)
2D classification
(CryoSPARC)
homogeneous refinement
(CryoSPARC)
3D variability analysis
(CryoSPARC)
heterogeneous refinement
(3 classes; CryoSPARC)
homogeneous refinement
(CryoSPARC)
3D variability analysis
(CryoSPARC)
heterogeneous refinement
(4 classes; CryoSPARC)
use output
as references
class B1
(25%)
class B2
(42%)
class B3
(33%)
use combined output
as references (A1-5 + C1-2);
target class C1
4,128,219 particles
heterogeneous refinement
(7 classes; CryoSPARC)
class C1
(33%)
class C2
(44%)
class C3
(23%)
2D classification
(CryoSPARC)
homogeneous refinement
(CryoSPARC/Relion)
3D classification with mask on
nucleosome (4 classes; Relion)
3D classification with mask on
hexasome/Chd1 (4 classes; Relion)
class D1
(21%)
class D2
(35%)
class D3
(25%)
class D4
(19%)
class E1
(30%)
class E2
(23%)
class E3
(23%)
class E4
(24%)
intersect; 26,819 particles
3D classification with mask on
DBD/DNA (2 classes; Relion)
particle subtraction
(Relion)
3D refinement
(Relion)
nucleosome
(4.0 Å)
hexasome/Chd1
(4.0 Å)
combine maps
(Warp)

Figure S13: **Image processing for the reconstruction of the Chd1-bound SHN103, related to Figure 4 and STAR Methods.** See STAR Methods for explanation.

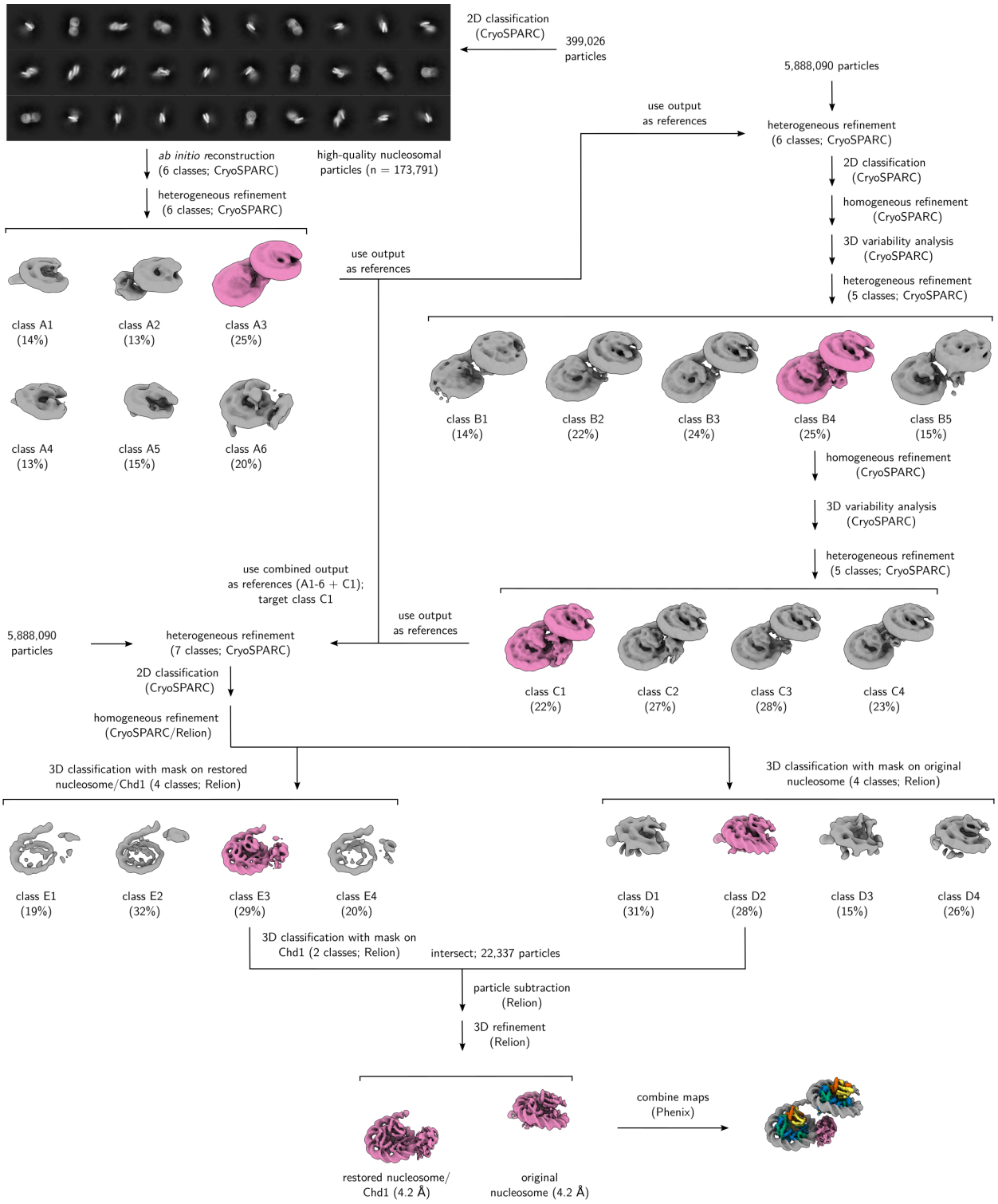
2D classification
(CryoSPARC)
399,026
particles
5,888,090 particles
use output
as references
heterogeneous refinement
(6 classes; CryoSPARC)
2D classification
(CryoSPARC)
homogeneous refinement
(CryoSPARC)
3D variability analysis
(CryoSPARC)
heterogeneous refinement
(5 classes; CryoSPARC)
ab initio reconstruction
(6 classes; CryoSPARC)
high-quality nucleosomal
particles (n = 173,791)
heterogeneous refinement
(6 classes; CryoSPARC)
use output
as references
class A1
(14%)
class A2
(13%)
class A3
(25%)
class A4
(13%)
class A5
(15%)
class A6
(20%)
class B1
(14%)
class B2
(22%)
class B3
(24%)
class B4
(25%)
class B5
(15%)
homogeneous refinement
(CryoSPARC)
3D variability analysis
(CryoSPARC)
heterogeneous refinement
(5 classes; CryoSPARC)
use combined output
as references (A1-6 + C1);
target class C1
use output
as references
5,888,090
particles
heterogeneous refinement
(7 classes; CryoSPARC)
2D classification
(CryoSPARC)
homogeneous refinement
(CryoSPARC/Relion)
class C1
(22%)
class C2
(27%)
class C3
(28%)
class C4
(23%)
3D classification with mask on restored
nucleosome/Chd1 (4 classes; Relion)
3D classification with mask on original
nucleosome (4 classes; Relion)
class E1
(19%)
class E2
(32%)
class E3
(29%)
class E4
(20%)
class D1
(31%)
class D2
(28%)
class D3
(15%)
class D4
(26%)
3D classification with mask on
Chd1 (2 classes; Relion)
intersect; 22,337 particles
particle subtraction
(Relion)
3D refinement
(Relion)
combine maps
(Phenix)
restored nucleosome/
Chd1 (4.2 Å)
original
nucleosome (4.2 Å)

Figure S14: **Image processing for the reconstruction of the Chd1-bound DN103, related to Figure 5 and STAR Methods.** See STAR Methods for explanation.

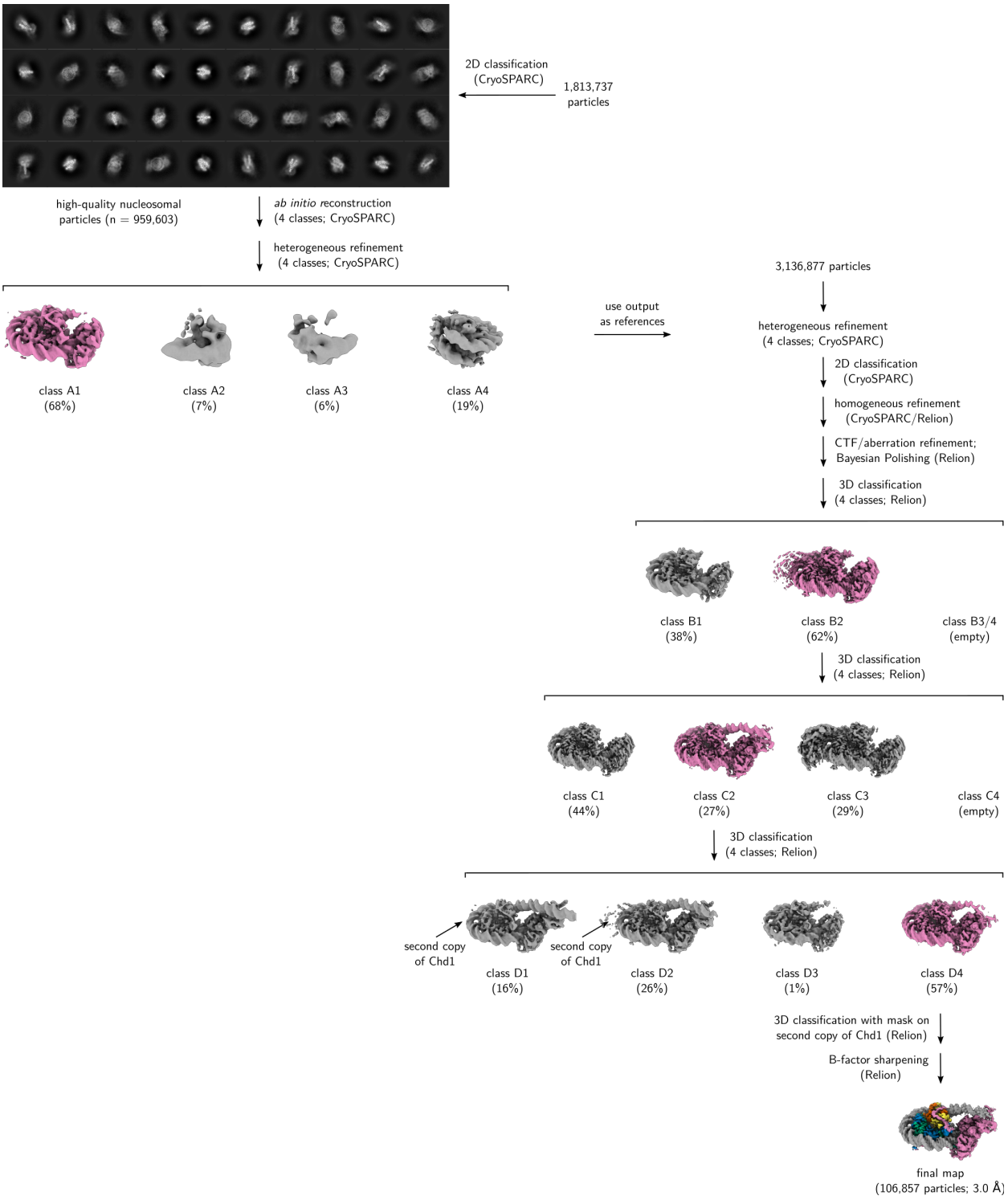
2D classification
(CryoSPARC)
1,813,737
particles
high-quality nucleosomal
particles (n = 959,603)
ab initio reconstruction
(4 classes; CryoSPARC)
heterogeneous refinement
(4 classes; CryoSPARC)
class A1
(68%)
class A2
(7%)
class A3
(6%)
class A4
(19%)
use output
as references
3,136,877 particles
heterogeneous refinement
(4 classes; CryoSPARC)
2D classification
(CryoSPARC)
homogeneous refinement
(CryoSPARC/Relion)
CTF/aberration refinement;
Bayesian Polishing (Relion)
3D classification
(4 classes; Relion)
class B1
(38%)
class B2
(62%)
class B3/4
(empty)
3D classification
(4 classes; Relion)
class C1
(44%)
class C2
(27%)
class C3
(29%)
class C4
(empty)
3D classification
(4 classes; Relion)
second copy
of Chd1
class D1
(16%)
second copy
of Chd1
class D2
(26%)
class D3
(1%)
class D4
(57%)
3D classification with mask on
second copy of Chd1 (Relion)
B-factor sharpening
(Relion)
final map
(106,857 particles; 3.0 Å)

Figure S15: **Image processing for the reconstruction of Chd1-bound 30W54, related to Figure S7 and STAR Methods.** See STAR Methods for explanation.

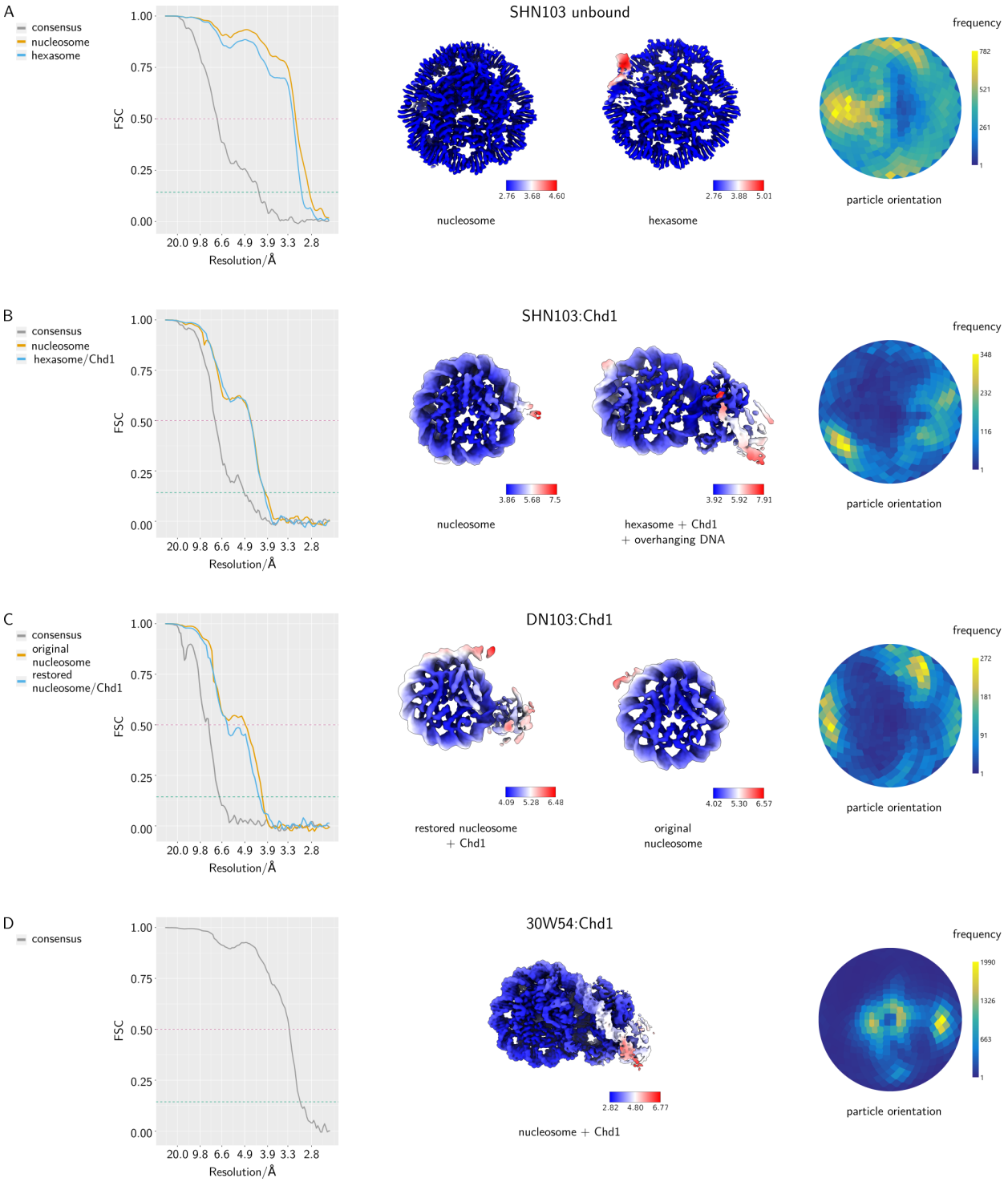
A
consensus
nucleosome
hexasome
FSC
1.00
0.75
0.50
0.25
0.00
20.0 9.8 6.6 4.9 3.9 3.3 2.8
Resolution/Å
SHN103 unbound
2.76 3.68 4.60
nucleosome
2.76 3.88 5.01
hexasome
frequency
782
521
261
1
particle orientation
B
consensus
nucleosome
hexasome/Chd1
FSC
1.00
0.75
0.50
0.25
0.00
20.0 9.8 6.6 4.9 3.9 3.3 2.8
Resolution/Å
SHN103:Chd1
3.86 5.68 7.5
nucleosome
3.92 5.92 7.91
hexasome + Chd1
+ overhanging DNA
frequency
348
232
116
1
particle orientation
C
consensus
original
nucleosome
restored
nucleosome/Chd1
FSC
1.00
0.75
0.50
0.25
0.00
20.0 9.8 6.6 4.9 3.9 3.3 2.8
Resolution/Å
DN103:Chd1
4.09 5.28 6.48
restored nucleosome
+ Chd1
4.02 5.30 6.57
original
nucleosome
frequency
272
181
91
1
particle orientation
D
consensus
FSC
1.00
0.75
0.50
0.25
0.00
20.0 9.8 6.6 4.9 3.9 3.3 2.8
Resolution/Å
30W54:Chd1
2.82 4.80 6.77
nucleosome + Chd1
frequency
1990
1326
663
1
particle orientation

Figure S16: **FSC curves and angular distributions, related to Figures 3, 4, 5 and S7.** (**A-D**) FSC curves (left), local resolution maps (midlle) and angular distribution plots (right) for the four different structures.

2 Supplemental Tables

	SHN103 unbound (PDB-9GD0)		**SHN103:Chd1** (PDB-9GD1)	
	nucleosome (EMDB-51239)	hexasome (EMDB-51240)	nucleosome (EMDB-51242)	hexasome:Chd1 (EMDB-51243)
Data collection and processing				
Microscope	FEI Titan Krios			
Voltage (kV)	300			
Camera	Gatan K3			
Magnification	105,000			
Pixel size at detector (Å)	0.834			
Total electron exposure ($e^-/Å^2$)	41.1		39.8	
Electron flux (e^-/pixel/s)	14.3		20.2	
Number of frames per exposure	40			
Defocus range (μm)	0.5 to 2.0			
Automation software	SerialEM			
Engergy filter slit width (eV)	20			
Micrographs collected (no.)	13,717		26,096	
Micrographs used (no.)	13,476		25,506	
Total extracted particle (no.)	4,245,216		4,128,219	
Reconstruction				
Refined particles (no.)	984,363		578,457	
Final particle (no.)	143,477		26,819	
Point-group symmetry	C1			
Resolution (global, Å)	2.8	3.0	4.0	4.0
FSC 0.5 (unmasked/masked)	8.1/3.1	8.0/3.2	7.4/4.6	7.4/4.5
FSC 0.143 (unmasked/masked)	4.0/2.8	4.2/3.0	4.6/4.0	4.6/4.0
Resolution range (local, Å)	2.8 to 4.6	2.8 to 5.0	3.9 to 7.5	3.9 to 7.9
Map sharpening B factor ($Å^2$)	-55.1	-50.2	-10.0	
Map sharpening methods	Local Refinement (CryoSPARC)		Post-processing (Relion)	
Model composition				
Protein residues	1253		2098	
DNA	500		518	
Ligands	0		MG, BEF, ADP	
B factors ($Å^2$)				
Protein	31.98		201.34	
DNA	105.94		252.26	
Ligand	n.a.		172.89	
R.m.s. deviations from ideal				
Bond length (Å)	0.006		0.005	
Bond angles (°)	0.842		0.825	
Validation				

MolProbity score	1.22	1.40
CaBLAM outliers	0.25	0.70
Clashscore	4.41	7.21
Poor rotamers (%)	0.00	0.39
Ramachandran plot		
Favored (%)	99.51	98.64
Allowed (%)	0.49	1.36
Disallowed (%)	0.0	0.0

Table S1: **Cryo-EM data collection, refinement and validation statistics for SHN103 unbound and SHN103:Chd1, related to Figures 3 and 4.**

	DN103:Chd1 (PDB-9GD2)		30W54:Chd1 (PDB-9GD3)
	original nucleosome (EMDB-51245)	restored nucleosome:Chd1 (EMDB-51246)	all (EMDB-51247)
Data collection and processing			
Microscope	FEI Titan Krios		
Voltage (kV)	300		
Camera	Gatan K3		
Magnification	105,000		
Pixel size at detector (Å)	0.834		
Total electron exposure ($e^-/Å^2$)	57.5		44.0
Electron flux (e^-/pixel/s)	29.7		20.4
Number of frames per exposure	40		60
Defocus range (μm)	0.5 to 2.0		
Automation software	SerialEM		
Engergy filter slit width (eV)	20		
Micrographs collected (no.)	34,271		9398
Micrographs used (no.)	33,346		8917
Total extracted particle (no.)	5,888,090		3,136,877
Reconstruction			
Refined particles (no.)	249,676		1,766,846
Final particle (no.)	22,337		106,857
Point-group symmetry	C1		
Resolution (global, Å)	4.2	4.2	3.0
FSC 0.5 (unmasked/masked)	7.0/4.9	7.3/6.1	4.3/3.3
FSC 0.143 (unmasked/masked)	4.5/4.2	4.7/4.2	3.3/3.0
Resolution range (local, Å)	4.0 to 6.6	4.1 to 6.5	2.8 to 6.8
Map sharpening B factor ($Å^2$)	-10.0		-50.6
Map sharpening methods	Post-processing (Relion)		
Model composition			
Protein residues	2104		1630
DNA	474		284
Ligands	MG, BEF, ADP		MG, BEF, ADP
B factors ($Å^2$)			
Protein	320.76		15.29
DNA	321.76		69.06
Ligand	358.28		5.53
R.m.s. deviations from ideal			
Bond length (Å)	0.006		0.005
Bond angles (°)	0.863		0.850
Validation			
MolProbity score	1.43		0.89
CaBLAM outliers	0.89		0.70
Clashscore	7.94		1.23

Poor rotamers (%)	0.94	0.07
Ramachandran plot		
Favored (%)	98.30	97.81
Allowed (%)	1.70	2.19
Disallowed (%)	0.0	0.0

Table S2: **Cryo-EM data collection, refinement and validation statistics for DN103:Chd1 and 30W54:Chd1, related to Figures 5 and S7.**

Structure	Centroid to Centroid[1]	Offset along SH normal[2]	Offset along dyad[3]	Angle between SH normals[4]	Angle between dyads[5]
SHN103 (cryo-EM)	60.4	-27.4	46.6	17.5	40.4
SHN103 (5gse)	45.4	-29.5	25.9	6.39	61.1
SHN103:Chd1	60.7	-25.3	46.9	18.0	35.3
DN103:Chd1	88.7	-72.9	10.6	32.7	3.7
SHN103:CHD4	53.1	-40.5	27.8	17.1	68.9

Table S3: **Geometry of SHN103 in the different structures, related to Figures 3, 4 and 5.**

[1]Distance between the centroids of the nucleosome and hexasome in Å.

[2]Offset between the centroid of the nucleosome and centroid of the hexasome projected onto the SH normal of the nucleosome in Å.

[3]Offset between the centroid of the nucleosome and centroid of the hexasome projected onto the dyad axis of the nucleosome in Å.

[4]Angle between the two SH normals in °.

[5]Angle between the nucleosome dyad axis and the hexasome dyad axis projected onto the nucleosome plane in °.

3 References

1. McGinty, R. K., and Tan, S. (2015). Nucleosome structure and function. Chem Rev *115*, 2255–73. 10.1021/cr500373h.

2. Henikoff, S., Ramachandran, S., Krassovsky, K., Bryson, T. D., Codomo, C. A., Brogaard, K., Widom, J., Wang, J.-P., and Henikoff, J. G. (2014). The budding yeast Centromere DNA Element II wraps a stable Cse4 hemisome in either orientation in vivo. Elife *3*, e01861. 10.7554/eLife.01861.

3. Pelechano, V., Wei, W., and Steinmetz, L. M. (2013). Extensive transcriptional heterogeneity revealed by isoform profiling. Nature *497*, 127–31. 10.1038/nature12121.

4. Xu, Y., Bernecky, C., Lee, C.-T., Maier, K. C., Schwalb, B., Tegunov, D., Plitzko, J. M., Urlaub, H., and Cramer, P. (2017). Architecture of the RNA polymerase II-Paf1C-TFIIS transcription elongation complex. Nat Commun *8*, 15741. 10.1038/ncomms15741.

5. Ocampo, J., Chereji, R. V., Eriksson, P. R., and Clark, D. J. (2019). Contrasting roles of the RSC and ISW1/CHD1 chromatin remodelers in RNA polymerase II elongation and termination. Genome Res. *29*, 407–417. 10.1101/gr.242032.118.

6. Kato, D., Osakabe, A., Arimura, Y., Mizukami, Y., Horikoshi, N., Saikusa, K., Akashi, S., Nishimura, Y., Park, S.-Y., Nogami, J., Maehara, K., Ohkawa, Y., Matsumoto, A., Kono, H., Inoue, R., Sugiyama, M., and Kurumizaka, H. (2017). Crystal structure of the overlapping dinucleosome composed of hexasome and octasome. Science *356*, 205–208. 10.1126/science.aak9867.

7. Vasudevan, D., Chua, E. Y. D., and Davey, C. A. (2010). Crystal structures of nucleosome core particles containing the '601' strong positioning sequence. J Mol Biol *403*, 1–10. 10.1016/j.jmb.2010.08.039.

8. Luger, K., Mäder, A. W., Richmond, R. K., Sargent, D. F., and Richmond, T. J. (1997). Crystal structure of the nucleosome core particle at 2.8 A resolution. Nature *389*, 251–60. 10.1038/38444.

9. Flaus, A., Luger, K., Tan, S., and Richmond, T. J. (1996). Mapping nucleosome position at single base-pair resolution by using site-directed hydroxyl radicals. Proc Natl Acad Sci U S A *93*, 1370–5. 10.1073/pnas.93.4.1370.

10. Wang, T., Liu, Y., Edwards, G., Krzizike, D., Scherman, H., and Luger, K. (2018). The histone chaperone FACT modulates nucleosome structure by tethering its components. Life Sci Alliance *1*, e201800107. 10.26508/lsa.201800107.